ARTICLE

A phenoxy-bridged trinuclear Ni(II) complex: synthesis, structural elucidation and molecular docking with viral proteins

Sunil Kumar[a], Mukesh Choudhary[a]*

[a] Department of Chemistry, National Institute of Technology Patna, Patna-800005 (Bihar) India.

[a.] *Corresponding author: mukesh@nitp.ac.in

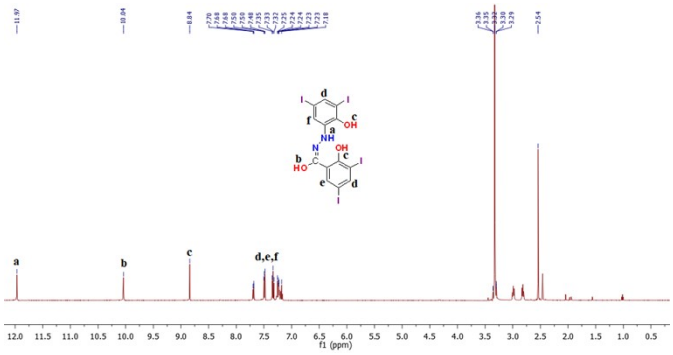

Figure S1. ^{1}H-NMR spectra of Schiff base ligand (H_3L).

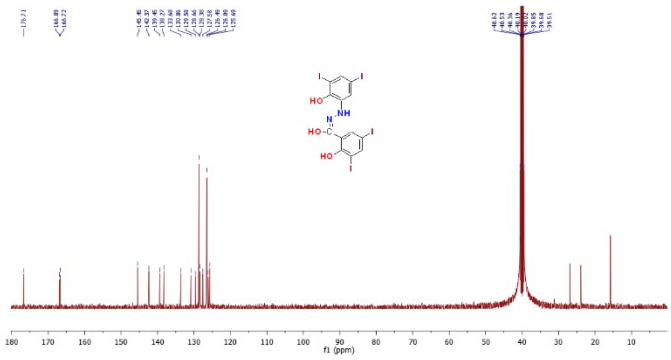

Figure S2 .^{13}C-NMR spectra of Schiff base ligand (H_3L).

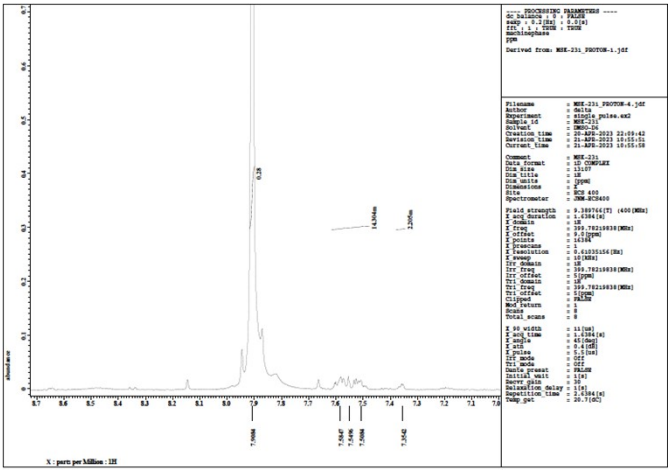

Figure S3. ^{1}H-NMR spectra of a phenoxy-bridged trinuclear nickel(II) complex $[Ni_3(\mu\text{-}L)_2(bipy)_3]$(**1**).

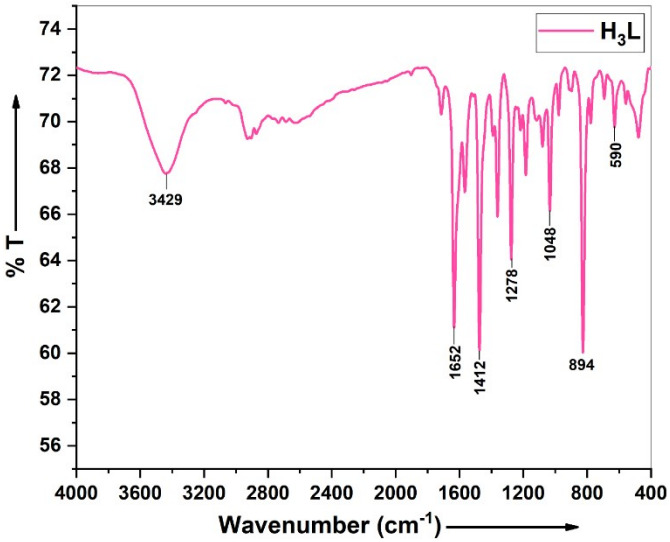

Figure S4. FT-IR spectra of the Schiff base ligand (H_3L).

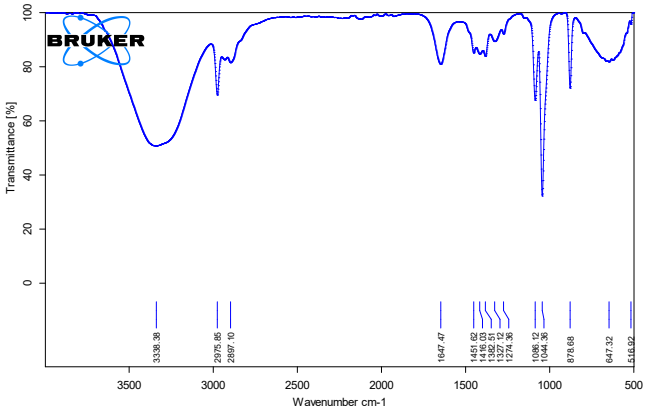

Figure S5. FT-IR spectra of a phenoxy-bridged trinuclear nickel(II) complex $[Ni_3(\mu\text{-}L)_2(bipy)_3]$(**1**).

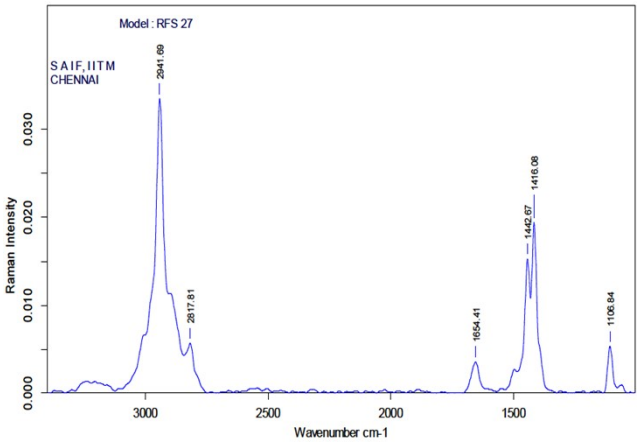

Figure S6. FT-Raman spectra of a phenoxy-bridged trinuclear nickel(II) complex $[Ni_3(\mu\text{-}L)_2(bipy)_3]$(**1**).

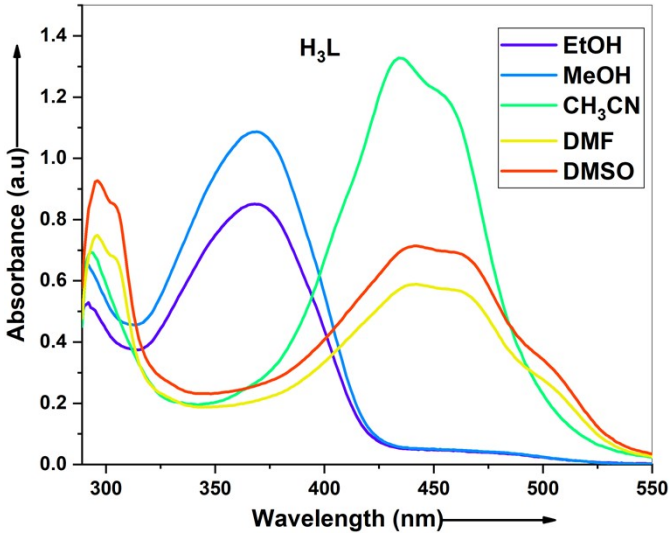

Figure S7. UV-Vis spectra of the Schiff base ligand (H_3L).

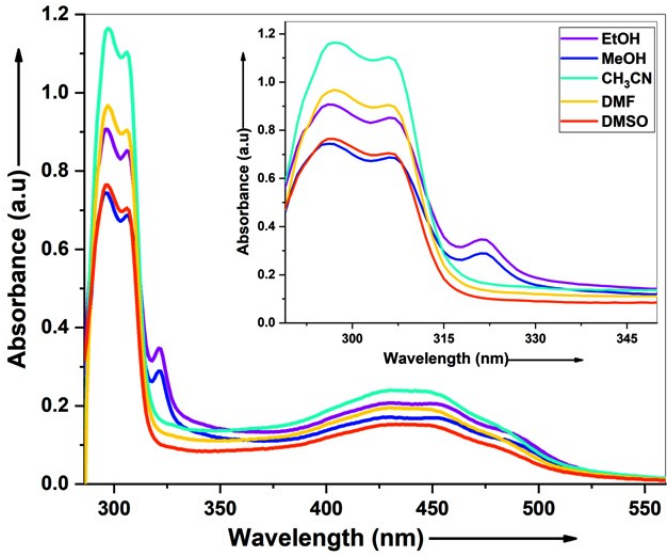

Figure S8. UV-Vis spectra of a phenoxy-bridged trinuclear nickel(II) complex $[Ni_3(\mu\text{-}L)_2(bipy)_3]$ (**1**).

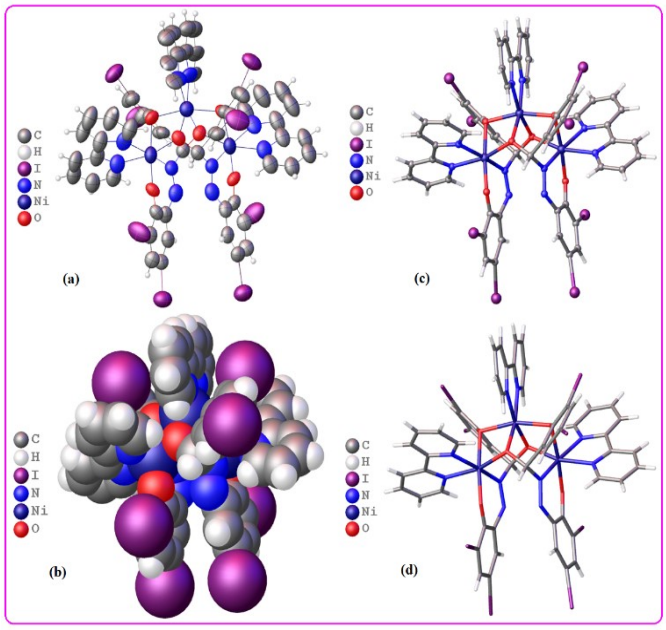

Figure S9. Perspective views of the molecular structures of a phenoxy-bridged trinuclear nickel(II) complex $[Ni_3(\mu\text{-}L)_2(bipy)_3]$(**1**) showing various models; (a) Ellipses and wireframe model, (b) Sphere Space-filling model, (c) ball & stick model and (d) Tube & stick model.

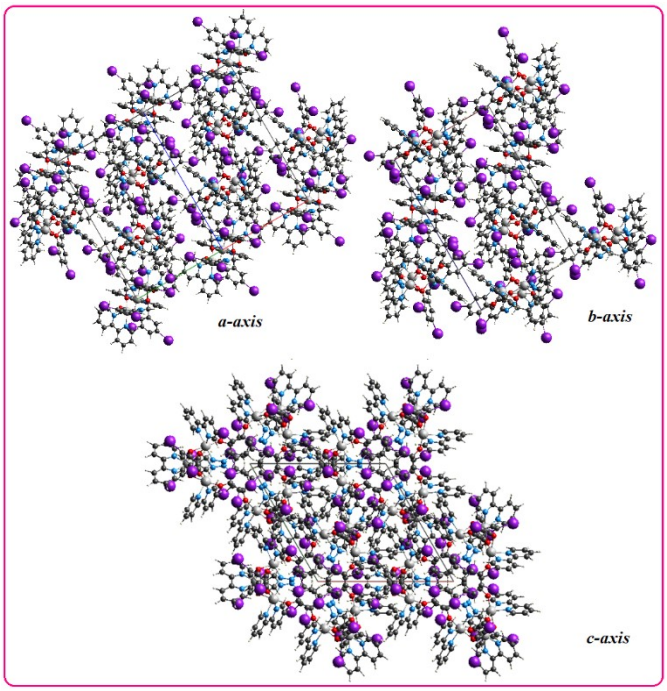

Figure S10. Packing view of a phenoxy-bridged trinuclear nickel(II) complex $[Ni_3(\mu\text{-}L)_2(bipy)_3]$(**1**) (along the *a*-*c*-axis).

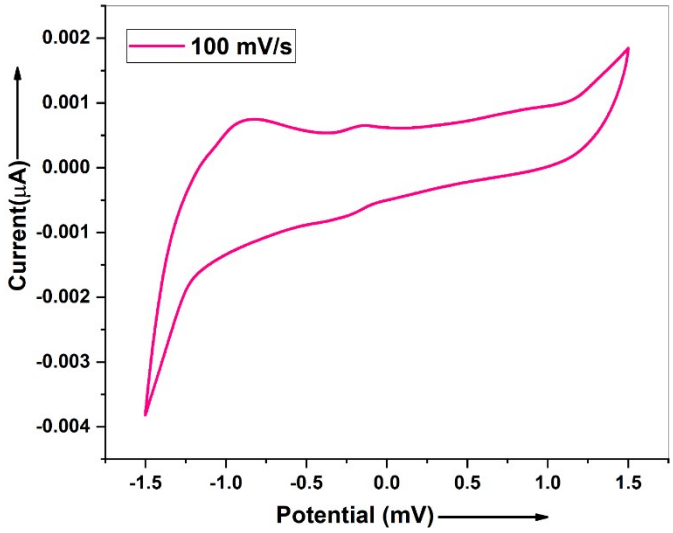

Figure S11. Cyclic voltammogram curve of a phenoxy-bridged trinuclear nickel(II) complex[$Ni_3(\mu\text{-}L)_2(bipy)_3$](**1**) with scan rate at 100 mV/s in DMSO with 1x10^{-3} M TBAP as supporting electrolyte.

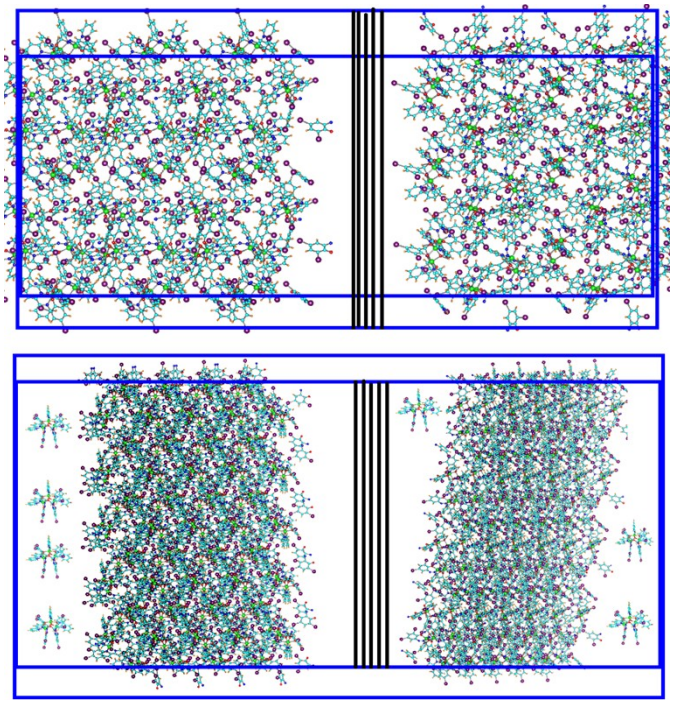

Figure S12. Pictorial view of typical initial and final configurations obtained from DFT quantum chemical calculations with the B3LYP method, as exemplified by phenoxy-bridged trinuclear nickel(II) complex [$Ni_3(\mu\text{-}L)_2(bipy)_3$](**1**).

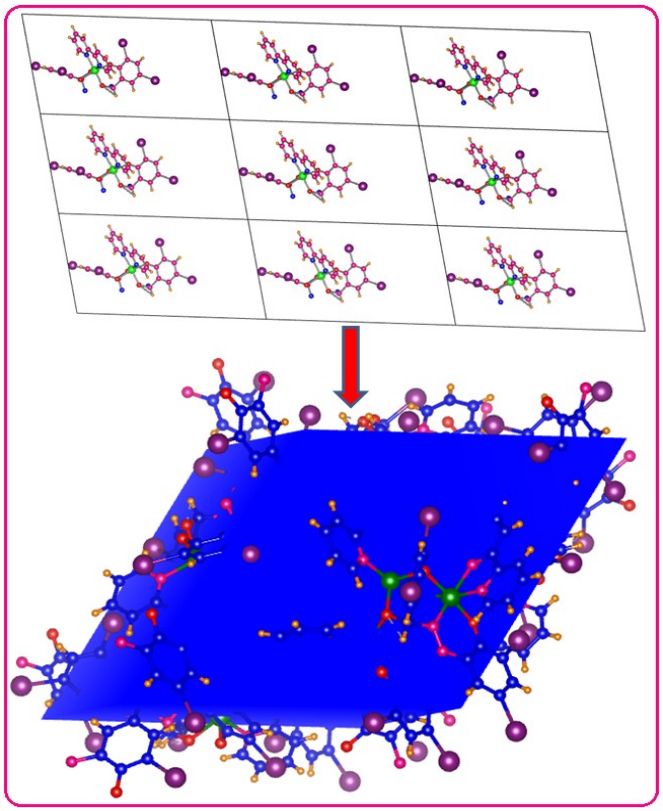

Figure S13. Representation of packing cell fragments into the Fourier synthesis transformation of a phenoxy-bridged trinuclear nickel(II) complex [$Ni_3(\mu\text{-}L)_2(bipy)_3$](**1**).

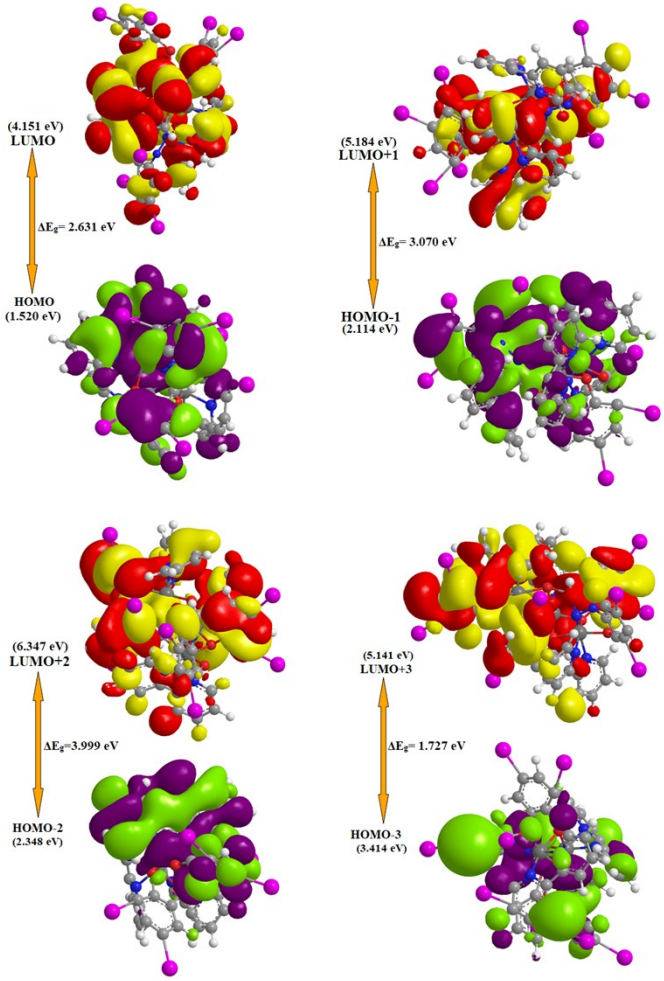

Figure S14. The atomic orbital composition of the frontier molecular orbitals of a phenoxy-bridged trinuclear nickel(II) complex $[Ni_3(\mu\text{-}L)_2(bipy)_3]$(**1**).

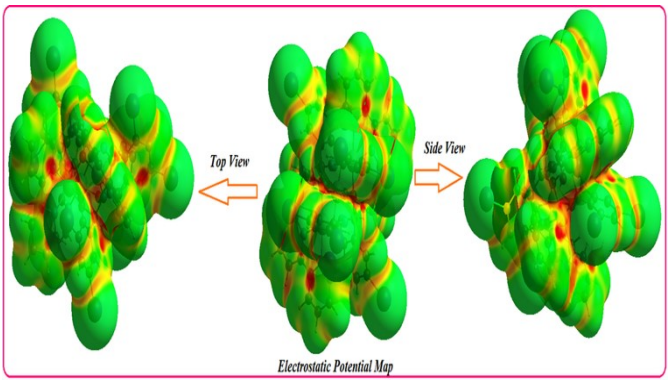

Figure S15. The molecular electrostatic potential maps (MEPs) of a phenoxy-bridged trinuclear nickel(II) complex $[Ni_3(\mu\text{-}L)_2(bipy)_3]$(**1**) with iso-value of 0.020 to 0.024 a.u., where negative potential decreases in order of red >orange >yellow >green.

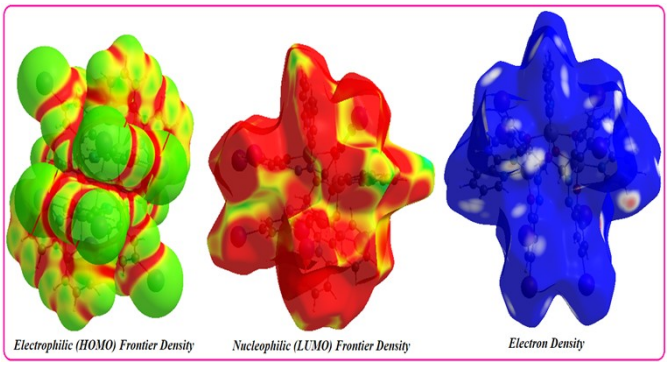

Figure S16. The molecular frontier density maps (MFPs) of a phenoxy-bridged trinuclear nickel(II) complex $[Ni_3(\mu\text{-}L)_2(bipy)_3]$(**1**) with iso-value of 0.020 to 0.024 a.u., where negative potential decreases in order of red > orange > yellow > green > blue.

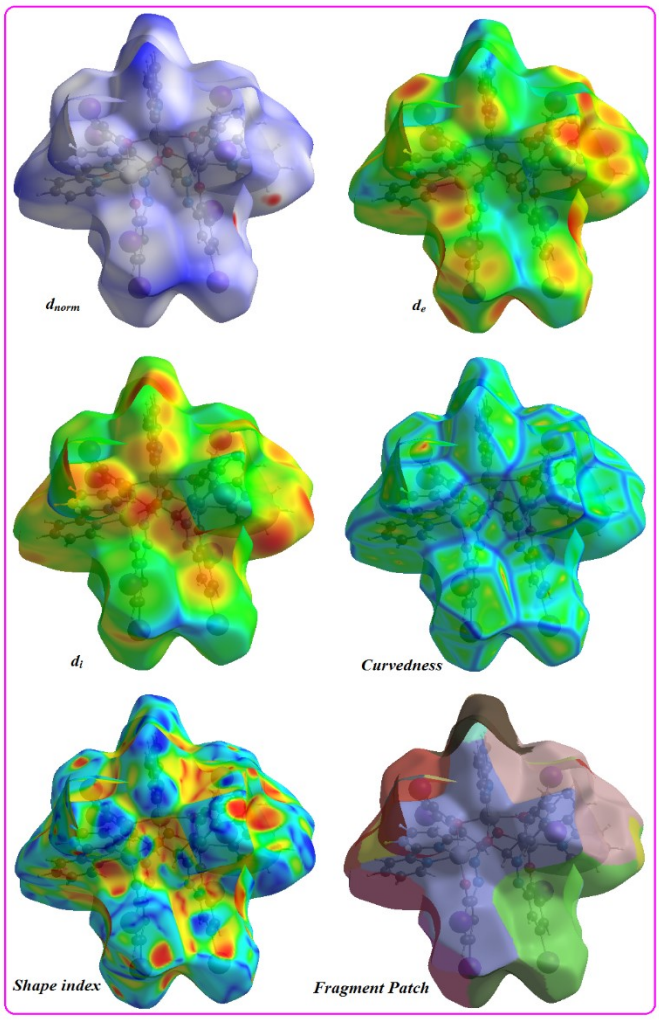

Figure S17. Graphical view (Full-portion) of the Hirshfeld surfaces of a phenoxy-bridged trinuclear nickel(II) complex $[Ni_3(\mu\text{-}L)_2(bipy)_3]$(**1**) mapped with d_{norm}, d_e, d_i, curvedness, shape index and Fragment patch; red spots represents the closest contacts and blue colour the most distant contacts.

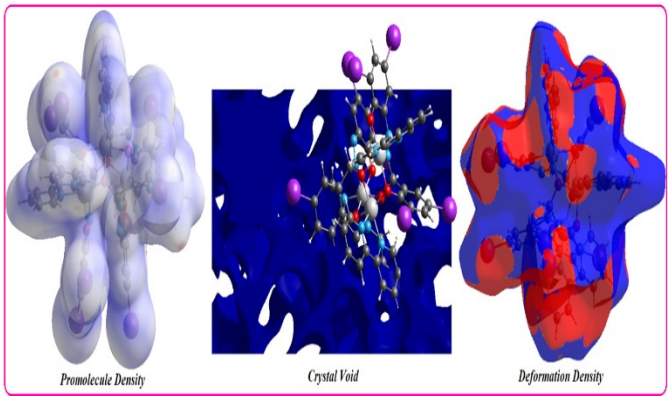

Figure S18. Graphical view of the Hirshfeld surfaces of a phenoxy-bridged trinuclear nickel(II) complex $[Ni_3(\mu\text{-}L)_2(bipy)_3]$(**1**) mapped with promolecule density, crystal void and deformation density; red spots represents the closest contacts and blue colour the most distant contacts.

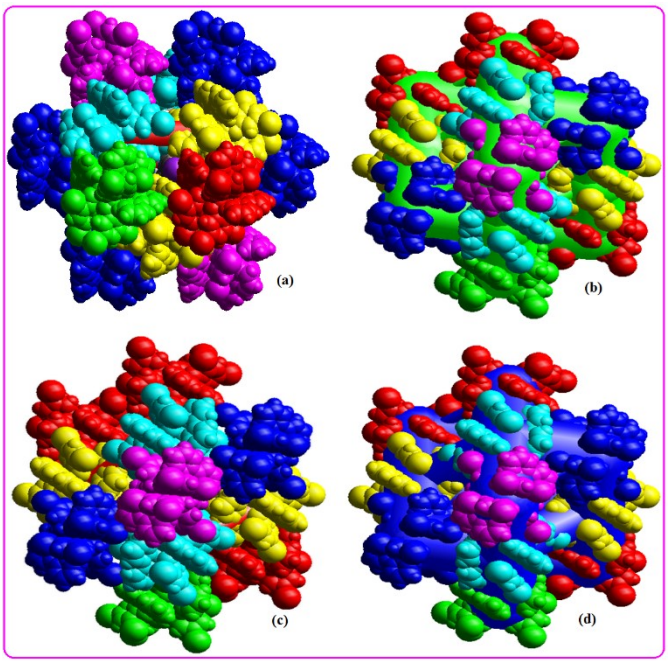

Figure S19. Space filling models of energy framework diagrams of a phenoxy-bridged trinuclear nickel(II) complex $[Ni_3(\mu\text{-}L)_2(bipy)_3]$(**1**); (a) Coulomb energy (E_{coul}), (b) Dispersion energy (E_{dis}), (c) Total energy (E_{tot}) and (d) Electrostatic energy (E_{elec}),for cluster of molecules. Hydrogen atoms have been omitted for clarity.

Figure S20. Computed CE-B3LYP estimates of energy components and total energies (kJ/mol) for the closest intermolecular interactions of a phenoxy-bridged trinuclear nickel(II) complex $[Ni_3(\mu\text{-}L)_2(bipy)_3]$(**1**).

	N	Symop	R	Electron Density	E_ele	E_pol	E_dis	E_rep	E_tot
	3	y, x, -z	17.79	HF/3-21G	1.9	-0.7	-8.9	0.0	-6.5
	4	-y, x-y, z+2/3	12.24	HF/3-21G	1.9	-8.7	-104.1	0.0	-97.5
	1	-y, x-y, z+2/3	17.79	HF/3-21G	1.6	-0.6	-8.9	0.0	-6.8
	2	y, x, -z	11.29	HF/3-21G	-24.7	-13.7	-116.0	63.2	-87.3
	4	x, y, z	16.08	HF/3-21G	-4.7	-2.1	-12.8	0.0	-17.7
	2	x, y, z	16.08	HF/3-21G	-32.3	-5.8	-41.3	0.0	-73.9

Scale factors for benchmarked energy models
See Mackenzie et al. IUCrJ (2017)

Energy Model	k_ele	k_pol	k_disp	k_rep
CE-HF ... HF/3-21G electron densities	1.019	0.651	0.901	0.811
CE-B3LYP ... B3LYP/6-31G(d,p) electron densities	1.057	0.740	0.871	0.618

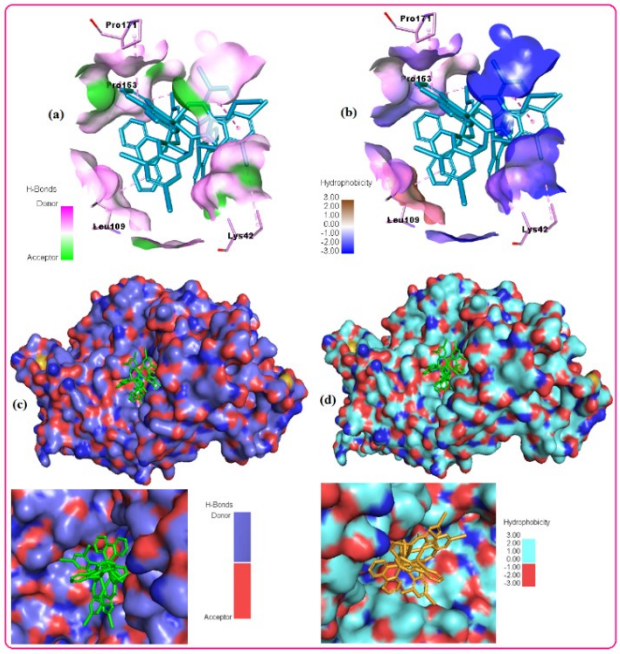

Figure S21. Graphical view of the total density surfaces representation of the docked phenoxy-bridged trinuclear nickel(II) complex $[Ni_3(\mu\text{-}L)_2(bipy)_3]$(**1**) inside the active site of the SARS-CoV-2 receptor binding domain (PDB ID: 7MZF); (a & b) with active site binding pocket of hydrogen bond donor and acceptor meshes represented by pink and green colours, respectively; (c & d) surface representation of hydrophobic active site binding pocket represented with blue and grey colours.

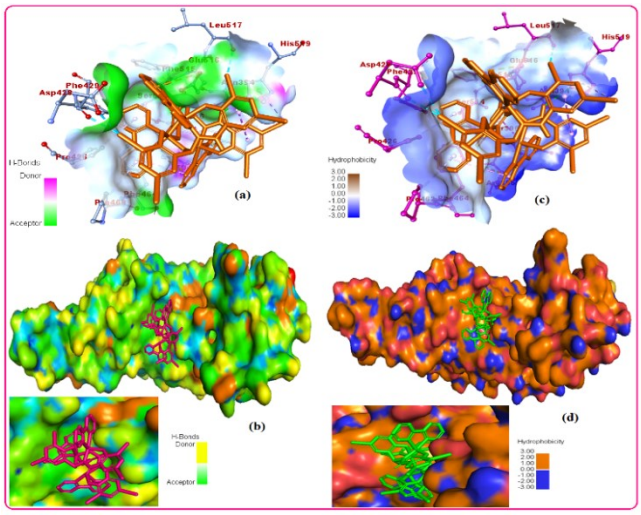

Figure S22. Graphical view of the total density surfaces representation of the docked phenoxy-bridged trinuclear nickel(II) complex $[Ni_3(\mu\text{-}L)_2(bipy)_3]$(**1**) inside the active site of the SARS-CoV-2 Omicron BA.3 variant spike protein (PDB ID: 7XIZ); (a & b) with active site binding pocket of hydrogen bond donor and acceptor meshes represented by pink and green colours, respectively; (c & d) surface representation of hydrophobic active site binding pocket represented with blue and grey colours.

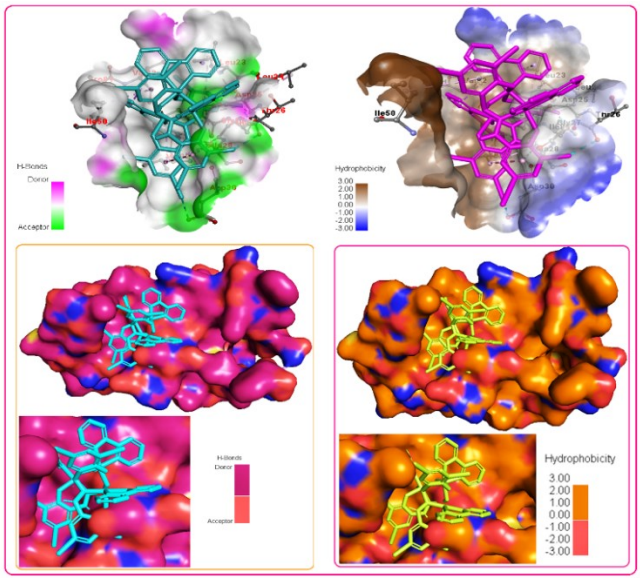

Figure S23. Graphical view of the total density surfaces representation of the docked phenoxy-bridged trinuclear nickel(II) complex $[Ni_3(\mu\text{-}L)_2(bipy)_3]$(**1**) inside the active site of the HIV-1 protease virus (PDB ID: 7WCQ); (a & b) with active site binding pocket of hydrogen bond donor and acceptor meshes represented by pink and green colours, respectively; (c & d) surface representation of hydrophobic active site binding pocket represented with blue and grey colours.

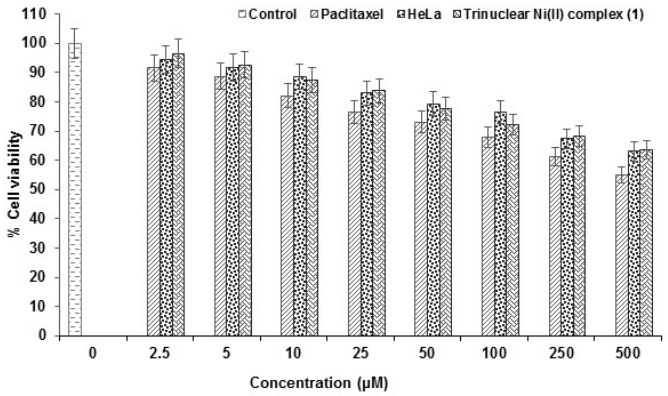

Figure S24. Percentage of Cell viability of HEK 293 and HeLa cells with increasing concentration of a trinuclear nickel(II) complex $[Ni_3(\mu\text{-}L)_2(bipy)_3]$(**1**) (0–500 μM) as quantified by MTT assay.

Table S1. Establishment of the structural activity relationship (SAR) between the bond lengths (Å) from X-ray crystallography of a trinuclear nickel(II) complex $[Ni_3(\mu\text{-}L)_2(bipy)_3]$(**1**) and theoretical data obtained from with SARS-CoV-2 RBD protein, Omicron BA.3 variant spike (PDB ID: 7XIZ) and HIV protease virus(PDB ID: 7WCQ) after molecular docking.

Complex	Bond	Exp. bond lengths (Å)	Theoretical bond lengths (Å)		
			(PDB ID: **7MZF**)	(PDB ID: **7XIZ**)	(PDB ID:**7WCQ**)
(**1**)	N(1)-Ni(1)	1.99(3)	1.98	1.98	1.99
	N(4)-Ni(1)	2.14(3)	2.13	2.13	2.15
	N(3)-Ni(1)	2.09(3)	2.07	2.08	2.09
	N(5)-Ni(2)	2.08(3)	2.10	2.07	2.09
	N(2)-N(1)	1.31(4)	1.29	1.29	1.30
	O(1)-Ni(2)	2.07(2)	2.06	2.05	2.08
	O(1)-Ni(1)	2.07(2)	2.08	2.07	2.06
	O(2)-Ni(2)	2.02(2)	2.01	2.03	2.02
	O(2)-Ni(1)#1	2.041(19)	2.041	2.043	2.042
	O(3)-Ni(1)	1.98(2)	1.97	1.97	1.98